ACS Energy Letters

Open Access
This article is licensed under CC-BY 4.0

pubs.acs.org/journal/aelccp
Letter

Mesoporous Carbon Hosts with Tailored Pore Structure for Lithium Deposition in Anode-Free All-Solid-State Batteries

Seung-Bo Hong, Young-Jun Lee, Hyeonseong Oh, A-Yeon Kim, Si Hyoung Oh, Kyung Yoon Chung, Dong-Won Kim,* Jieun Lee,* and Hun-Gi Jung*

Cite This: *ACS Energy Lett.* 2026, 11, 5051−5060

Read Online

ACCESS | Metrics & More | Article Recommendations | Supporting Information

ABSTRACT: Anode-free sulfide all-solid-state lithium batteries have emerged as a platform for achieving increased energy density. However, their practical operation is limited by heterogeneous interfacial reactions and uneven lithium deposition, which degrade reversibility and cycling stability. Among various approaches, silver−carbon (Ag−C) interlayers have attracted attention owing to their lithiophilicity and alloying behavior. Despite these advances, the role of carbon pore architecture in governing lithium deposition remains unclear. Here, we engineer mesoporous carbon hosts with tailored pore sizes to regulate the spatial distribution of Ag nanoparticles, thereby controlling Ag−C interfacial contact in anode-free sulfide ASSLBs. Systematic pore-size tuning promotes a more uniform distribution of Ag−C interfacial contact sites and enables homogeneous lithium deposition. Consequently, the pore-engineered host delivers enhanced cycling stability. This work establishes a clear structure−function relationship between carbon pore architecture and lithium deposition behavior, providing design guidelines for anode-free solid-state batteries.

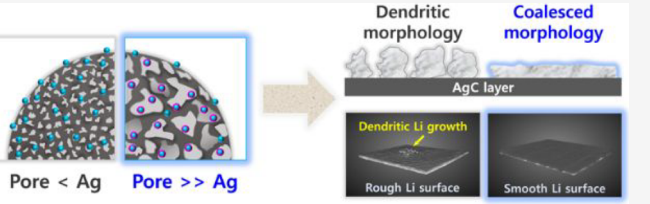

All-solid-state lithium batteries (ASSLBs) are widely regarded as next-generation energy storage systems owing to their enhanced safety and high energy density.[1,2] In particular, sulfide solid electrolytes, with their high ionic conductivity ($\sim 10^{-2}$ S cm^{-1}) and favorable mechanical deformability, enable intimate interfacial contact and practical cell designs with improved electrochemical performance.[3−11] To fully leverage these advantages, electrode architectures that maximize lithium utilization while minimizing inactive components are essential at the cell level. Among various approaches, anode-free configurations, which eliminate preloaded lithium at the anode, represent an effective strategy for further increasing energy density.[12] However, their practical implementation remains challenging. Non-uniform ionic transport and parasitic interfacial reactions can induce localized lithium accumulation, leading to poor cycling stability.[13−15] Therefore, regulating lithium deposition and stabilizing electrode−electrolyte interfaces are critical for durable anode-free ASSLBs.

To mitigate these challenges, several interfacial strategies have been proposed, including metal sputtering layers, conversion-type nanoparticle layers, and solid electrolyte modification.[16−27] Among them, carbon-based hosts are particularly attractive because they provide high electronic conductivity and surface-mediated Li transport pathways.[28−30] On this basis, carbon−metal composites incorporating lithiophilic metals such as Ag exhibit improved lithium nucleation and interfacial kinetics.[12,31−35] In silver−carbon (Ag−C) systems, Ag serves as the lithiophilic alloying component, and Li−Ag alloying promotes stable lithium deposition.[33] The carbon phase supports lithium transport and redistribution, the spatial organization of Ag nanoparticles within the interlayer, and structural buffering by physically separating the solid electrolyte from plated Li. Despite these reported improvements, prior discussions have largely focused on the lithiophilicity and alloying behavior of metallic components, whereas the structural characteristics of the carbon host remain comparatively underexplored.[32] Specifically, morphological factors such as pore size, pore connectivity, and interfacial contact geometry critically govern the spatial distribution of Ag−C contact sites, lithium transport pathways, and deposition behavior. Notably, these effects cannot be rationalized solely by the nominal surface area, as lithium transport and deposition are governed by the spatial accessibility of active interfaces and the resulting Li flux distribution within the carbon framework. However, the structure−property relationship within Ag−C systems remains unclear, and rational design guidelines for stabilizing lithium deposition through precise control of the carbon microstructure are still lacking.

In this study, we present a pore-size engineering strategy for mesoporous carbon hosts to elucidate the role of carbon microstructure in governing lithium deposition behavior in anode-free sulfide ASSLBs. Mesoporous architectures are adopted to control

Received: March 30, 2026
Revised: May 31, 2026
Accepted: June 1, 2026
Published: June 12, 2026

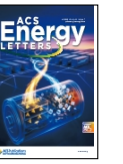

Downloaded via HANYANG UNIV on July 12, 2026 at 22:52:37 (UTC).
See https://pubs.acs.org/sharingguidelines for options on how to legitimately share published articles.

ACS Publications
© 2026 The Authors. Published by American Chemical Society

https://doi.org/10.1021/acsenergylett.6c00964
ACS Energy Lett. 2026, 11, 5051−5060

the size compatibility between Ag nanoparticles and carbon pores, thereby regulating the effective Ag−C interfacial contact that governs alloy-mediated Li deposition. By employing carbon frameworks with controlled pore sizes of 10, 30, and 150 nm in combination with Ag nanoparticles (∼20 nm), we demonstrate that pore accessibility is a key determinant of effective Ag−C interfacial contact and alloy-mediated lithium exchange. Pores smaller than the Ag nanoparticles restrict internal infiltration of Ag, limiting Ag−C interfacial contact and resulting in localized lithium flux and inhomogeneous deposition. In contrast, sufficiently large pores enable more distributed Ag−C contact and homogeneous lithium deposition. Consequently, the optimized architecture delivers stable interfacial deposition and markedly improved cycling stability. These findings establish a clear structure−function relationship between carbon pore architecture and lithium metal deposition behavior, providing rational design guidelines for durable anode-free solid-state batteries.

To systematically investigate the influence of Ag−C interfacial contact on Li−Ag alloying and subsequent lithium deposition behavior, three mesoporous carbons with distinct pore sizes were designed as model hosts (Figure S1). The samples, denoted as Carbon010, Carbon030, and Carbon150 according to their nominal pore sizes, were characterized by nitrogen adsorption−desorption isotherms and Brunauer−Emmett−Teller (BET) measurements to quantify their pore structures and surface areas (Figures S2 and S3). Scanning electron microscopy (SEM) and transmission electron microscopy (TEM) observations reveal that Carbon010 exhibits a densely wrinkled surface with a fine pore network (∼10 nm), whereas Carbon030 shows a more open morphology with uniformly distributed mesopores (∼30 nm). In contrast, Carbon150 presents an expanded framework with pores spanning tens to hundreds of nanometers. Consistent with these structural variations, the BET surface areas decrease from 1223 to 608 and 190 m^2 g^{-1} for Carbon010, Carbon030, and Carbon150, respectively, reflecting the inverse relationship between BET surface area and pore size. These structural differences provide an important basis for interpreting subsequent Ag−C composite behavior. Specifically, the accessible interfacial

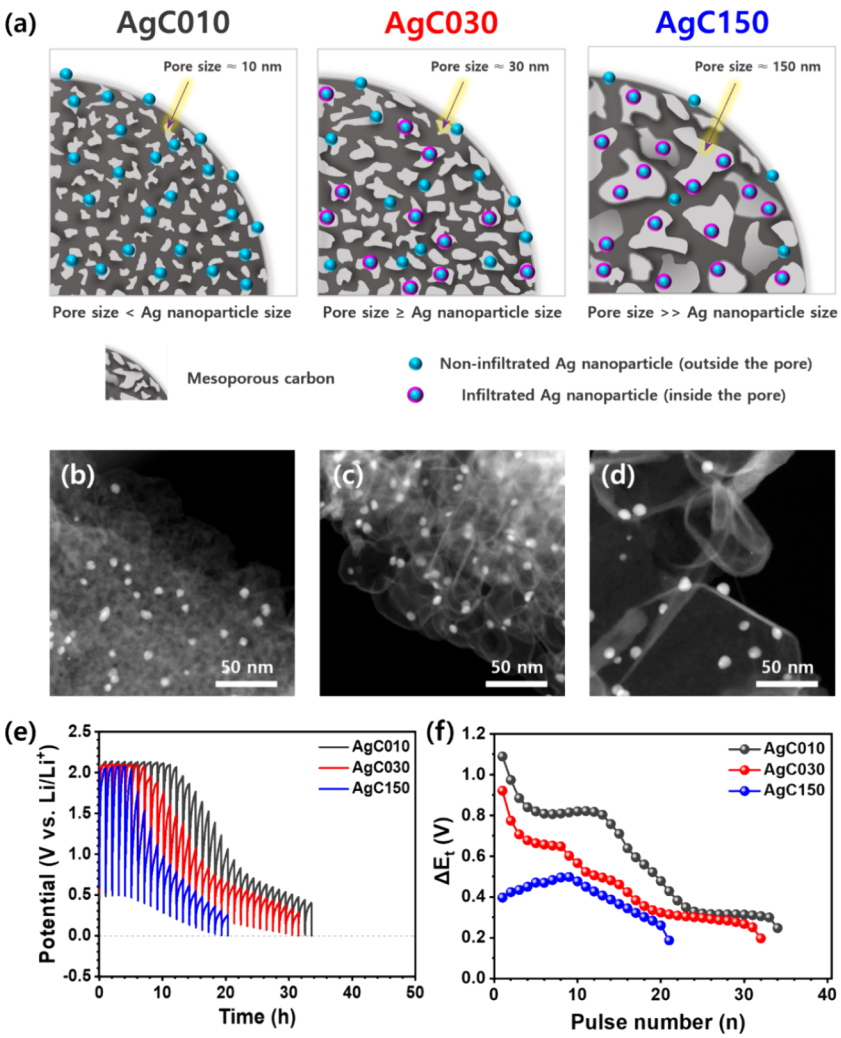

Figure 1. (a) Schematic illustration showing the distribution of Ag nanoparticles in AgC010, AgC030, and AgC150 as a function of mesoporous carbon pore size. Depending on the relative sizes of the pore and Ag nanoparticles, Ag particles are preferentially located either on the external surface or inside the mesopores. HAADF-TEM images of (b) AgC010, (c) AgC030, and (d) AgC150, visualizing the distribution of Ag nanoparticles within the mesoporous carbon frameworks. (e) Voltage profiles of Li/Ag−C half cells with different carbon hosts during stepwise galvanostatic current pulses. (f) Within-pulse polarization ($\Delta E_t = E_{0+} - E_\tau$) as a function of pulse number. Here, E_{0+} is the first recorded potential after current application and E_τ is the potential at the end of the 1 min pulse.

https://doi.org/10.1021/acsenergylett.6c00964
ACS Energy Lett. 2026, 11, 5051−5060

area available for Ag nanoparticles (~20 nm), rather than nominal surface area alone, is expected to govern effective Ag−C contact and interfacial reactions. Accordingly, these carbons serve as ideal model hosts to examine how pore architecture governs Ag−C interactions and the resulting lithium deposition behavior.

The distribution of Ag nanoparticles within the mesoporous carbon hosts is summarized schematically and experimentally in Figure 1. According to the pore size of the parent carbons, the composites are denoted as AgC010, AgC030, and AgC150. As illustrated in the scheme, when the pore size is smaller than the Ag nanoparticle diameter (~20 nm), as in AgC010, Ag nanoparticles are primarily restricted to the external surface (Figure 1a). In contrast, with increasing pore size in AgC030 and AgC150, a progressively larger fraction of Ag nanoparticles infiltrates into the mesoporous framework and contacts the internal carbon surfaces. This trend is corroborated by TEM imaging together with EDS elemental mapping (Figures 1b−d and S4). AgC010 shows Ag nanoparticles predominantly located on the outer surface, whereas AgC030 and AgC150 exhibit increasing populations of particles distributed within the internal pore network, with the most pronounced internal incorporation observed for AgC150. To further distinguish particle locations, backscattered electron (BSE) SEM imaging was employed (Figure S5). Owing to the higher atomic number of Ag relative to carbon, Ag nanoparticles appear with brighter contrast in BSE mode, enabling selective visualization of their spatial distribution.[31] A combined analysis of secondary electron (SE) and BSE imaging provides complementary morphological and compositional contrast, allowing clear identification of the carbon framework and reliable differentiation between particles located inside and outside the mesopores. This comparison reveals a systematic increase in internally located Ag nanoparticles with increasing pore size. These structural observations suggest that, beyond the total surface area, the accessible interfacial area available for Ag infiltration governs the extent of Ag−C contact.

To examine the pre-activation behavior of the Ag−C interlayers prior to lithium deposition, galvanostatic intermittent titration technique (GITT) measurements were performed starting from the open-circuit voltage (Figure 1e).[32,36] Repeated current pulses (1 mA cm^{-2}, 1 min) gradually lowered the potential toward 0 V, corresponding to the transition from carbon lithiation to the onset of lithium deposition. Because carbon lithiation consumes lithium without directly contributing to reversible bulk Li plating, the amount of lithium consumed during this pre-deposition region is governed by the surface area of the carbon host. AgC150 reached this endpoint earlier than AgC010 and AgC030, indicating that less Li reservoir is consumed by carbon lithiation. To compare the polarization under identical current pulses, we defined within-pulse polarization as ΔEt ($= E_{0+} - E_{\tau}$), where E_{0+} is the first recorded potential after current application and E_{τ} is the potential at the end of the pulse (Figure S6). ΔE_t captures the additional polarization accumulated during the pulse, which is sensitive to the effective reaction and transport distribution within the interlayer. ΔE_t decreased from AgC010 to AgC150, resulting in the smallest ΔE_t for AgC150 (Figure 1f), suggesting more homogeneous reaction and transport kinetics within the interlayer enabled by more internally distributed Ag−C contact.

Electrochemical cycling tests were conducted to compare the lithium plating behavior of the three Ag−C composite electrodes

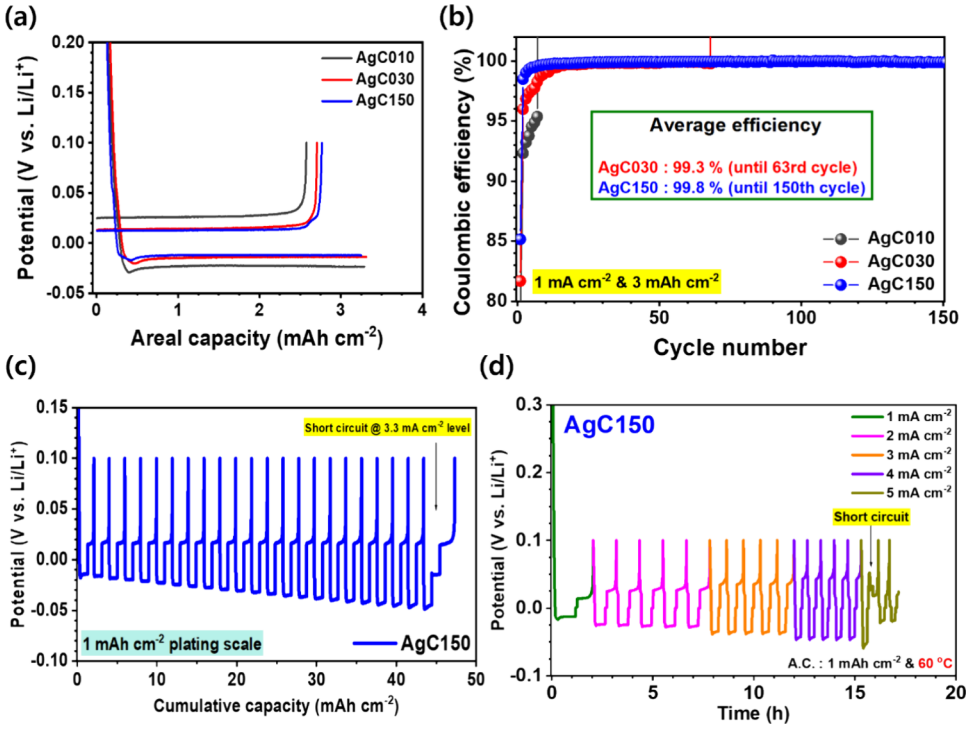

Figure 2. (a) First cycle charge-discharge voltage profiles and (b) corresponding coulombic efficiencies over repeated cycles of Li/AgC010, Li/AgC030, and Li/AgC150 cells measured at a current density of 1 mA cm^{-2} with an areal capacity of 3 mAh cm^{-2} at 60 °C. (c) Voltage response of the Li/AgC150 cell plotted as a function of cumulative areal capacity under stepwise increased plating current densities, while maintaining a fixed areal capacity of 1 mAh cm^{-2}. (d) Critical current density test of the Li/AgC150 cell, in which both plating and stripping current densities were increased stepwise while maintaining a fixed areal capacity of 1 mAh cm^{-2}.

https://doi.org/10.1021/acsenergylett.6c00964
ACS Energy Lett. 2026, 11, 5051−5060

under identical conditions. Both plating and stripping were performed at a current density of 1 mA cm^{-2} with a fixed deposition capacity of 3 mAh cm^{-2}. The first cycle voltage−capacity profiles reveal a transient potential drop at the onset of plating, followed by a stable plateau (Figure 2a). This feature corresponds to the nucleation overpotential, which reflects the interfacial lithiophilicity and the energy barrier for lithium nucleation.[16,33] A magnified view of the early plating region shows that AgC150 exhibits the smallest nucleation overpotential, followed by AgC030 and AgC010, suggesting that pore architecture and Ag−C interfacial characteristics influence the initial nucleation behavior (Figure S7). To identify the preferential lithium deposition location, cross-sectional SEM analyses were performed (Figure S8). The deposited lithium was identified as an Ag-enriched Li−Ag alloy phase, formed during lithium plating. In all cases, lithium deposition occurred at the interface between the SUS current collector and the Ag−C interlayer, while no deposition was observed at the interface between the Ag−C interlayer and the solid electrolyte pellet. These observations suggest that the subsequent plating behavior is primarily governed by the properties of the Ag−C interlayer. The spatial distribution of Ag nanoparticles after the plating−stripping process was examined by TEM (Figure S9). Following the first electrochemical cycle, the Ag−C interlayers were collected and sonicated. Because sonication preferentially removes weakly attached particles from the external surface, while particles confined within internal pores are relatively retained, this treatment provides a simple means to distinguish externally attached Ag from those stabilized inside the mesoporous structure. Notably, distinct Ag signals were still observed in AgC030 and AgC150 after sonication, indicating the presence of nanoparticles retained within the internal pore network. In contrast, Ag signals were barely detectable in AgC010, suggesting that most particles were located on the outer surface and were removed during the sonication process. These results indicate that carbon hosts with sufficiently large pores effectively confine and retain

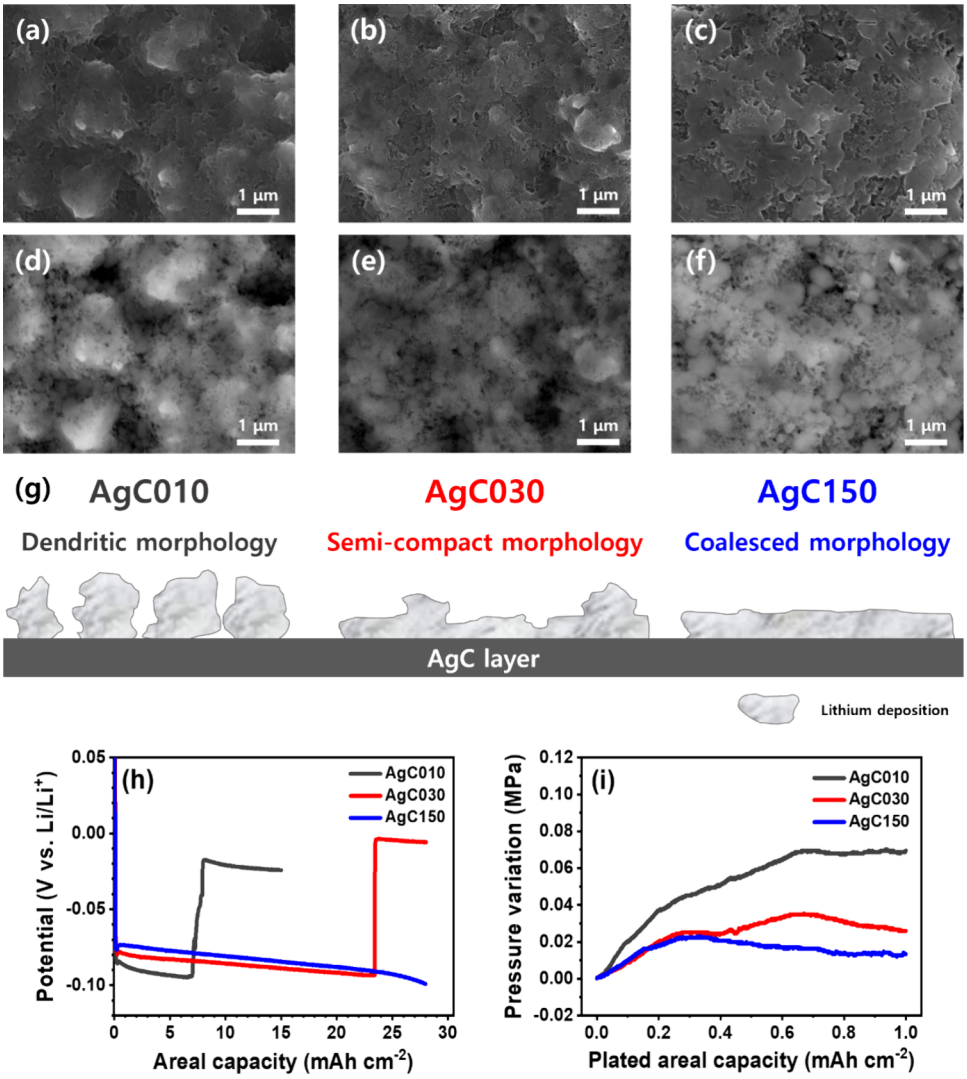

Figure 3. Top-view SEM images of Li deposited on AgC anodes to an areal capacity of 0.3 mAh cm^{-2}. SE-mode SEM images of Li deposited on (a) AgC010, (b) AgC030, and (c) AgC150. Corresponding BSE-mode SEM images of (d) AgC010, (e) AgC030, and (f) AgC150, respectively. (g) Schematic illustration summarizing the representative Li deposition morphologies based on the SEM observations. (h) Voltage profiles during extended Li plating on AgC electrodes at an elevated current density of 5 mA cm^{-2} under continuous deposition until short-circuit. (i) Pressure variation profiles measured during the initial stage of Li plating as a function of plated areal capacity.

https://doi.org/10.1021/acsenergylett.6c00964
ACS Energy Lett. 2026, 11, 5051−5060

Ag nanoparticles within the internal framework, thereby helping to sustain reversible alloying reactions within the Ag−C interlayer during subsequent cycling. On this basis, the long-term electrochemical behavior of the cells was evaluated. Cycling was continued under the same conditions, and the evolution of coulombic efficiency is summarized in Figure 2b. AgC010 exhibited consistently lower coulombic efficiency from the initial cycles and failed at an earlier stage due to short-circuiting, whereas AgC030 showed improved stability. Notably, AgC150 maintained the highest average coulombic efficiency with stable long-term cycling. The corresponding voltage profiles are provided in Figures S10 and S11. To further assess interfacial robustness under higher lithium flux, the plating current density was progressively increased while maintaining a fixed areal capacity.[19] Stable voltage responses were sustained over a wider current range for AgC150, whereas AgC010 and AgC030 failed at lower currents (Figures 2c and S12). Finally, the critical current density (CCD) values were compared by simultaneously increasing both plating and stripping current densities.[27] AgC010 and AgC030 exhibited early failure at limited current densities, while AgC150 preserved stable voltage profiles over substantially higher current levels, demonstrating superior kinetic tolerance and interfacial stability (Figures 2d and S13). To isolate the contribution of Ag incorporation, the electrochemical behavior of the mesoporous carbon hosts without Ag was also evaluated under identical conditions (1 mA cm^{-2}, 3 mAh cm^{-2}) (Figure S14). A more detailed discussion on the respective roles of the carbon network and Ag−C interactions is provided in the Supporting Information (Supplementary Note 1).

The morphology of lithium plated on the Ag−C interlayers was examined to correlate electrochemical performance with deposition characteristics. The electrodes were recovered after the initial plating stage at 0.3 mAh cm^{-2} and subsequently observed by top-view SEM (Figure 3a−f). SE mode SEM images reveal distinct differences in deposition uniformity among the three electrodes.[31,37−39] AgC010 exhibits localized lithium accumulation with growth concentrated at discrete spots, indicative of nonuniform nucleation and dendritic propagation. AgC030 displays a more continuous morphology but still exhibits partially dendritic features, whereas AgC150 presents a markedly homogeneous and laterally distributed lithium layer with reduced protrusions, suggesting uniform surface coverage. These contrasts become more apparent in the corresponding BSE mode SEM images. Because BSE contrast scales with atomic number, Ag-containing Li−Ag alloy regions appear brighter than carbon in BSE mode, enabling selective visualization of the deposited phase. AgC010 shows sparse bright domains separated by large dark regions, reflecting incomplete surface coverage, while AgC150 exhibits uniformly distributed bright contrast across most of the surface, consistent with continuous and compact lithium deposition. A schematic illustration summarizes this evolution from dendritic growth (AgC010) to semi-compact structures (AgC030) and finally to coalesced, laterally merged morphologies (AgC150) (Figure 3g). These observations suggest that increased internal Ag−C contact promotes a more homogeneous lithium flux, favoring lateral growth over localized accumulation.

The deposition behavior was further evaluated under continuous plating conditions to assess interfacial stability at higher current densities.[40] To enable a more stringent comparison, the cells were tested under a controlled stack pressure (6 MPa) at an elevated current density (5 mA cm^{-2}), imposing harsher plating conditions that accentuate differences in lithium growth morphology. Voltage profiles recorded during extended lithium plating show that AgC010 short-circuits rapidly, whereas AgC150 sustains stable operation over a substantially larger plated capacity (Figure 3h). The early failure of AgC010 is consistent with localized and dendritic growth, while the prolonged stability of

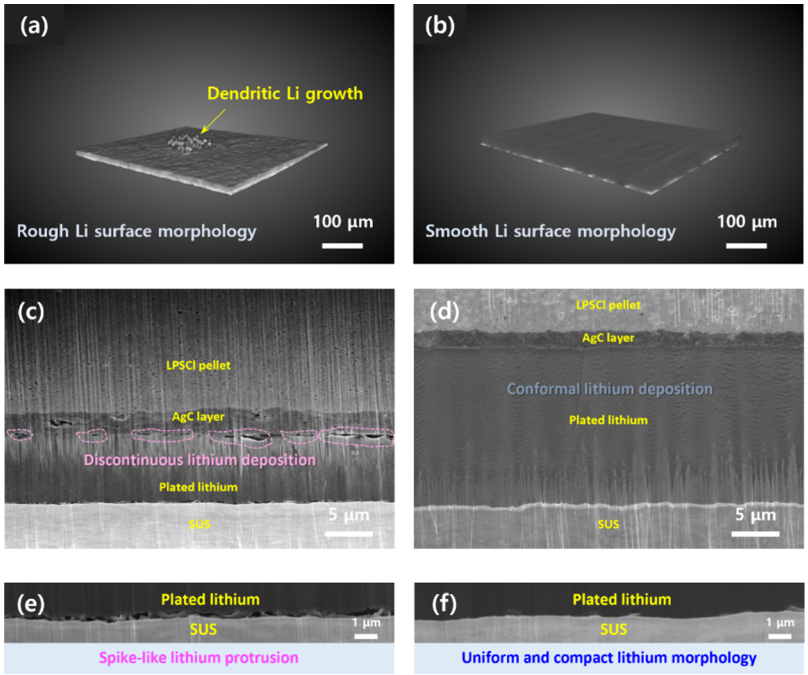

Figure 4. 3D XRM images of Li/AgC cells after electrochemical cycling: (a) Li/AgC030 cell after 60 cycles and (b) Li/AgC150 cell after 100 cycles. Cross-sectional FIB-SEM images of (c), (e) Li/AgC030 cell after 60 cycles and (d), (f) Li/AgC150 cell after 100 cycles. The analysis points were selected to capture representative interfacial morphologies before severe cell failure in the less stable configuration.

https://doi.org/10.1021/acsenergylett.6c00964
ACS Energy Lett. 2026, 11, 5051−5060

AgC150 indicates more uniform and laterally distributed deposition. Pressure variation was simultaneously monitored using pressiometry to probe the mechanical response associated with lithium growth. Electrodes exhibiting dendritic or vertically protruding deposits are expected to induce larger pressure fluctuations, whereas laterally spreading deposition leads to more gradual pressure changes. Consistent with this expectation, AgC010 shows the largest pressure variation, while AgC150 exhibits the smallest and most stable response (Figure 3i). These trends corroborate the morphological observations and indicate that enlarged Ag−C interfacial contact promotes lateral lithium growth and mitigates dendritic lithium accumulation.

After prolonged cycles, post-mortem structural analyses were performed to directly visualize the evolution of the Ag−C interlayers and to correlate the observed electrochemical stability with morphological integrity. Three-dimensional X-ray microscopy (XRM) was first employed to non-destructively examine the internal architecture of the electrodes.[17,19] Post-mortem analyses were conducted on AgC030 after 60 cycles and AgC150 after 100 cycles, respectively. The XRM images reveal a stark contrast between the two samples. In AgC030, a rough and highly irregular lithium surface is clearly observed, with distinct dendritic protrusions extending from the Ag−C interlayer, indicating localized and unstable deposition (Figure 4a). These dendritic features are readily visible across the electrode surface and reflect nonuniform lithium accumulation during cycling. By contrast, AgC150 exhibits a smooth and continuous lithium morphology without noticeable dendritic growth (Figure 4b). The deposited lithium forms a relatively flat and conformal layer, suggesting more homogeneous and laterally distributed deposition throughout the electrode. Cross-sectional focused ion beam (FIB) SEM analyses were subsequently performed to further resolve the interfacial lithium morphology. Consistent with the XRM observations, AgC030 exhibits discontinuous lithium deposition with interfacial gaps between the plated lithium and the Ag−C interlayer, together with spike-like protrusions preferentially extending toward the SUS current collector (Figure 4c,e). These features suggest deposition instability arising from spatially heterogeneous Li transport, uneven Li−Ag alloy-mediated nucleation, and interfacial contact evolution during repeated plating and stripping. Localized Li flux can promote spike-like Li growth during plating, while repeated volume changes and chemo-mechanical stress accumulation can lead to interfacial contact loss, stripping-induced void formation, or partial delamination.[41] Once such gaps

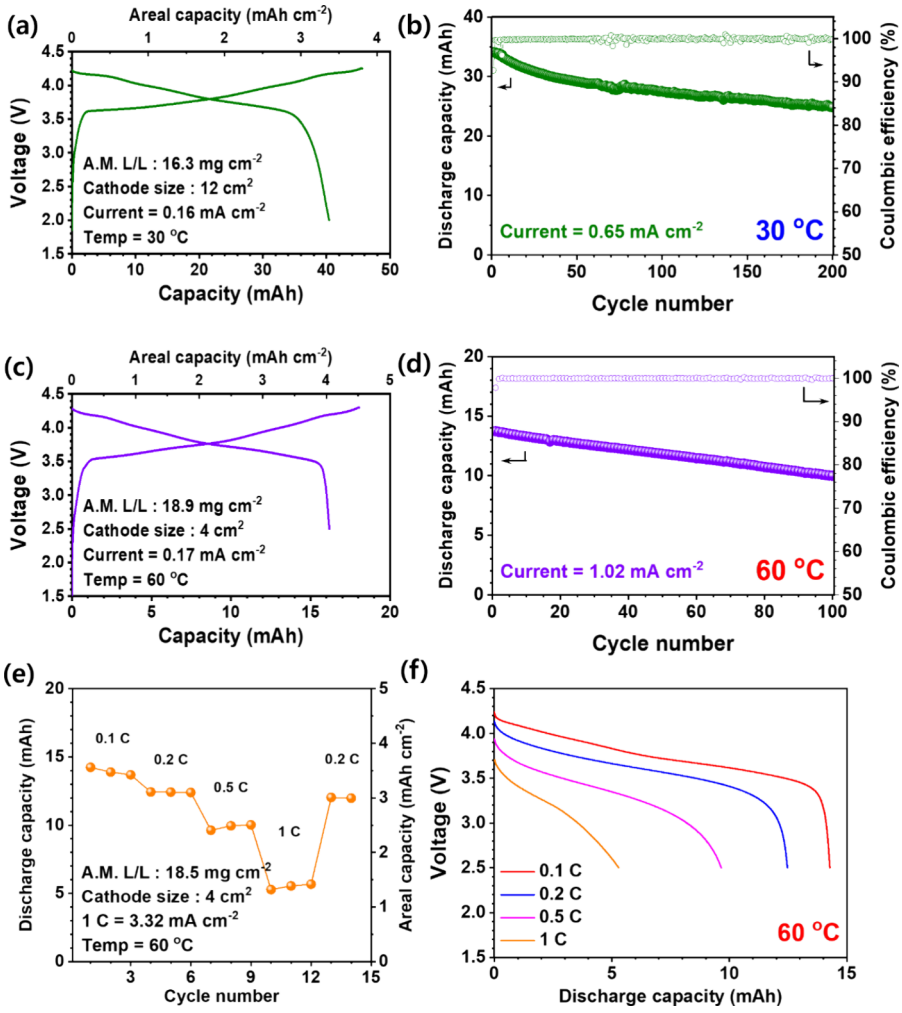

Figure 5. Electrochemical performance of pouch-type all-solid-state full cells employing AgC150 electrodes. (a) Initial voltage profile and (b) cycling performance of the 12 cm^2 pouch cell evaluated at 30 °C. (c) Initial voltage profile and (d) cycling performance of the 4 cm^2 pouch cell evaluated at 60 °C. Insets in (b) and (d) show the corresponding coulombic efficiencies during cycling. (e) Rate capability of the 4 cm^2 pouch cell evaluated at 60 °C and (f) corresponding discharge voltage profiles at various C-rates.

https://doi.org/10.1021/acsenergylett.6c00964
ACS Energy Lett. 2026, 11, 5051−5060

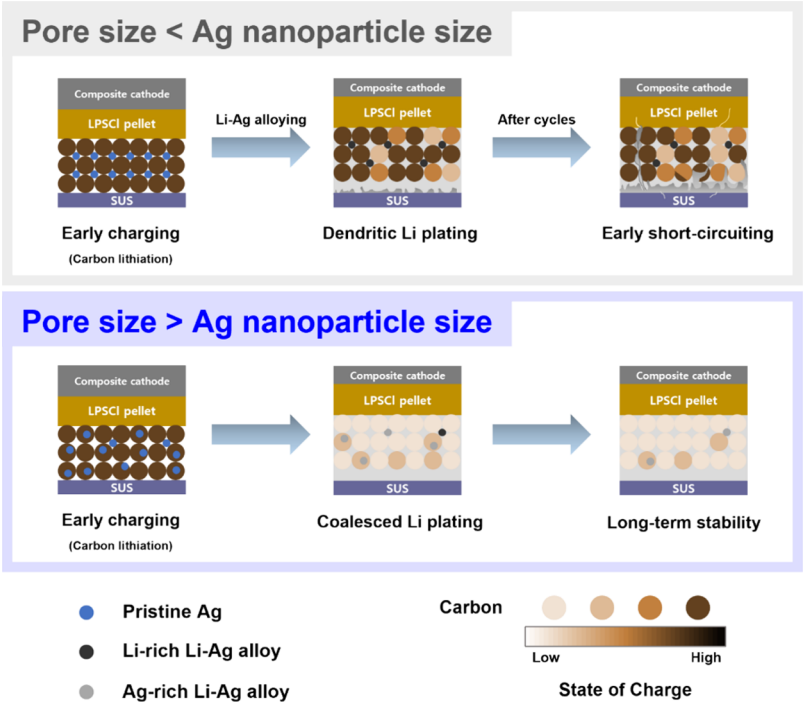

Figure 6. Schematic illustration of the relationship between carbon pore size and Ag nanoparticle size, and its impact on Li deposition behavior and cycling stability.

form, effective contact area becomes further restricted, concentrating the current at the remaining contact points, thereby accelerating localized deposition and interfacial instability. Thus, the interfacial gaps and spike-like protrusions are both a consequence and an indicator of deposition instability governed by coupled transport, interfacial contact, and chemo-mechanical effects. In contrast, AgC150 shows a dense and conformal lithium layer that more uniformly covers the Ag−C interlayer (Figure 4d,f). The deposited lithium forms a compact and continuous morphology with a well-maintained interface across the architecture.

To demonstrate the practical applicability of the Ag−C interlayer design, pouch-type full cells were assembled and evaluated under realistic operating conditions (Figures 5 and S15). Two types of pouch configurations with different cathode areas were prepared to assess both large-format scalability and high-rate performance.[42] For the large-area configuration employing a 12 cm^2 composite cathode, cycling tests were conducted at 30 °C, retaining 73 % of the initial capacity over 200 cycles (Figures 5a,b and S16a). The corresponding volumetric and gravimetric energy densities were calculated to be 657.0 Wh L^{-1} and 285.2 Wh kg^{-1}, respectively (Table S1). To further evaluate cell performance under more demanding conditions, a smaller-area pouch cell with a 4 cm^2 composite cathode was tested at 60 °C (Figures 5c−f and S16b).[43] Notably, higher energy densities of 781.5 Wh L^{-1} and 362.3 Wh kg^{-1} were achieved under these conditions (Table S1). These results demonstrate that the Ag−C interlayer architecture enables robust lithium utilization and stable cycling not only in laboratory-scale half cells but also in practical pouch-type full-cell configurations.

Figure 6 illustrates the mechanistic framework linking carbon pore size to Ag distribution and lithium deposition behavior in Ag−C interlayers. When the carbon pore size is smaller than the Ag nanoparticle diameter, Ag remains largely on the external carbon surface, resulting in spatially uneven Li−Ag alloy formation and localized current distribution during cycling. In contrast, pores larger than the Ag nanoparticle enable direct and distributed contact between Ag and the internal carbon surface, allowing Li−Ag alloying to be activated more uniformly through the lithiated carbon framework. This more homogeneous alloying pathway leads to a more evenly distributed lithium flux and favors lateral lithium deposition, which is consistent with the improved cycling stability and suppressed dendritic behavior observed across the electrochemical and morphological analyses.

In this study, we identify carbon pore size as a key structural parameter governing the functionality of Ag−C interlayers in sulfide-based anode-free all-solid-state lithium batteries. Small pores confine Ag nanoparticles to the external carbon surface, leading to unstable lithium deposition and early short-circuiting. In contrast, sufficiently large pores allow Ag to be more effectively incorporated into the carbon framework, thereby promoting stable lithium deposition under prolonged cycling and high-current-density conditions. Ag−C architectures with well-controlled pore structures demonstrate robust electrochemical performance from half-cell configurations to practical pouch-type full cells, highlighting the critical role of pore-size control in regulating lithium deposition behavior. By establishing a clear structure−function relationship between pore accessibility and Ag distribution, this work provides practical design guidelines for engineering durable Ag−C interlayers and advancing anode-free sulfide all-solid-state batteries.

■ ASSOCIATED CONTENT

Supporting Information

The Supporting Information is available free of charge at https://pubs.acs.org/doi/10.1021/acsenergylett.6c00964.

Supporting Information Available: Experimental method, Morphological characterization of mesoporous carbons

https://doi.org/10.1021/acsenergylett.6c00964
ACS Energy Lett. 2026, 11, 5051−5060

with different pore sizes, including SEM and TEM images of Carbon010, Carbon030, and Carbon150, Pore size distributions of mesoporous carbons with different nominal pore sizes, N_2 adsorption−desorption isotherms and corresponding BET plots of mesoporous carbons, BF-TEM images and corresponding HAADF-TEM with EDS elemental mapping of AgC samples with different pore sizes, Secondary electron and backscattered electron SEM images of AgC samples with different pore sizes, Determination of ΔE_t from GITT profiles, Enlarged voltage−areal capacity profiles during initial lithiation, Cross-sectional SEM images and corresponding EDS elemental maps of Li/AgC cells after initial Li plating, BF-TEM, HAADF-STEM with Ag EDS mapping, and corresponding HAADF-STEM images of AgC samples after the first Li plating/stripping cycle, Long-term Li plating/stripping voltage profiles of Li/AgC cells, Voltage profiles of Li/AgC half cells at different cycles, Stepwise current density tests and corresponding voltage responses of Li/AgC cells, Critical current density measurements of Li/AgC cells under stepwise current increase, Charge−discharge voltage profiles and enlarged initial lithiation behavior and corresponding coulombic efficiencies of Li/carbon cells, Photographs of pouch-type full cells, Charge−discharge voltage profiles of pouch-type all-solid-state cells at different temperatures, Calculation details for the energy density of all-solid-state pouch cells, Checklist of experimental details in this work (DOCX)

■ AUTHOR INFORMATION

Corresponding Authors

Dong-Won Kim – *Department of Chemical Engineering, Hanyang University, Seoul 04763, Korea; Department of Battery Engineering, Hanyang University, Seoul 04763, Korea;* orcid.org/0000-0002-1735-0272; Email: dongwonkim@hanyang.ac.kr

Jieun Lee – *Energy Storage Research Center, Sustainable Energy Research Division, Korea Institute of Science and Technology, Seoul 02792, Korea;* orcid.org/0000-0003-4227-4125; Email: jieunlee23@kist.re.kr

Hun-Gi Jung – *Energy Storage Research Center, Sustainable Energy Research Division, Korea Institute of Science and Technology, Seoul 02792, Korea; Division of Energy & Environment Technology, KIST School, Korea Institute of Science and Technology, Seoul 02792, Korea; Department of Energy Science and KIST-SKKU Carbon-Neutral Research Center, Sungkyunkwan University, Suwon 16419, Korea;* orcid.org/0000-0002-2162-2680; Email: hungi@kist.re.kr

Authors

Seung-Bo Hong – *Energy Storage Research Center, Sustainable Energy Research Division, Korea Institute of Science and Technology, Seoul 02792, Korea*

Young-Jun Lee – *Department of Chemical Engineering, Hanyang University, Seoul 04763, Korea*

Hyeonseong Oh – *Energy Storage Research Center, Sustainable Energy Research Division, Korea Institute of Science and Technology, Seoul 02792, Korea*

A-Yeon Kim – *Energy Storage Research Center, Sustainable Energy Research Division, Korea Institute of Science and Technology, Seoul 02792, Korea*

Si Hyoung Oh – *Energy Storage Research Center, Sustainable Energy Research Division, Korea Institute of Science and Technology, Seoul 02792, Korea; Division of Energy & Environment Technology, KIST School, Korea Institute of Science and Technology, Seoul 02792, Korea;* orcid.org/0000-0002-7063-9235

Kyung Yoon Chung – *Energy Storage Research Center, Sustainable Energy Research Division, Korea Institute of Science and Technology, Seoul 02792, Korea; Division of Energy & Environment Technology, KIST School, Korea Institute of Science and Technology, Seoul 02792, Korea;* orcid.org/0000-0002-1273-746X

Complete contact information is available at: https://pubs.acs.org/doi/10.1021/acsenergylett.6c00964

Notes

The authors declare no competing financial interest.

■ ACKNOWLEDGMENTS

S.-B. Hong and Y.-J. Lee contributed equally to this study. This work was supported by the National Research Council of Science & Technology (NST) grant by the Korea government (MSIT) (No. GTL24012-000), the National Research Foundation of Korea (NRF) funded by the Ministry of Science and ICT (No. RS-2025-23523434), and the Korea Institute of Science and Technology (KIST) Institutional Program (26E0322). This work was also supported by the National Research Foundation of Korea (RS-2024-00454354).

■ REFERENCES

(1) Janek, J.; Zeier, W. G. Challenges in Speeding Up Solid-State Battery Development. *Nat. Energy* **2023**, *8*, 230−240.

(2) Banerjee, A.; Wang, X.; Fang, C.; Wu, E. A.; Meng, Y. S. Interfaces and Interphases in All-Solid-State Batteries with Inorganic Solid Electrolytes. *Chem. Rev.* **2020**, *120*, 6878−6933.

(3) Kato, Y.; Hori, S.; Saito, T.; Suzuki, K.; Hirayama, M.; Mitsui, A.; Yonemura, M.; Iba, H.; Kanno, R. High-Power All-Solid-State Batteries Using Sulfide Superionic Conductors. *Nat. Energy* **2016**, *1*, No. 16030.

(4) Son, J. P.; Kim, J.-S.; Lee, C.-G.; Park, J.; Kim, J. S.; Kim, S.-H.; Gault, B.; Seo, D.-H.; Jung, Y. S. Dual-Function ZnO-Li_3TaO_4 Surface Modification of Single-Crystalline Ni-Rich Cathodes for All-Solid-State Batteries. *ACS Energy Lett.* **2024**, *9*, 5403−5412.

(5) Xiao, Y.; Wang, Y.; Bo, S.-H.; Kim, J. C.; Miara, L. J.; Ceder, G. Understanding Interface Stability in Solid-State Batteries. *Nat. Rev. Mater.* **2020**, *5*, 105−126.

(6) Woo, J.; Song, Y. B.; Kwak, H.; Jun, S.; Jang, B. Y.; Park, J.; Kim, K. T.; Park, C.; Lee, C.; Park, K.-H.; Lee, H.-W.; Jung, Y. S. Liquid-Phase Synthesis of Highly Deformable and Air-Stable Sn-Substituted Li_3PS_4 for All-Solid-State Batteries Fabricated and Operated under Low Pressures. *Adv. Energy Mater.* **2023**, *13*, No. 2203292.

(7) Hong, S.-B.; Lee, Y.-J.; Lee, H.-J.; Sim, H.-T.; Lee, H.; Lee, Y. M.; Kim, D.-W. Exploring the Cathode Active Materials for Sulfide-Based All-Solid-State Lithium Batteries with High Energy Density. *Small* **2024**, *20*, No. 2304747.

(8) Jang, B.; Lee, J.; Jung, Y. S. Solvent Footprint in Wet-Chemical Processing of Sulfide Solid Electrolytes for All-Solid-State Batteries. *ACS Energy Lett.* **2026**, *11*, 1169−1181.

(9) Hong, S.-B.; Jang, Y.-R.; Kim, H.; Jung, Y.-C.; Shin, G.; Hah, H. J.; Cho, W.; Sun, Y.-K.; Kim, D.-W. Wet-Processable Binder in Composite

Cathode for High Energy Density All-Solid-State Lithium Batteries. *Adv. Energy Mater.* **2024**, *14*, No. 2400802.

(10) Lee, J.; Lee, T.; Char, K.; Kim, K. J.; Choi, J. W. Issues and Advances in Scaling up Sulfide-Based All-Solid-State Batteries. *Acc. Chem. Res.* **2021**, *54*, 3390−3402.

(11) Tan, D. H. S.; Meng, Y. S.; Jang, J. Scaling up high-energy-density sulfidic solid-state batteries: A lab-to-pilot perspective. *Joule* **2022**, *6*, 1755−1769.

(12) Lee, Y.-G.; Fujiki, S.; Jung, C.; Suzuki, N.; Yashiro, N.; Omoda, R.; Ko, D.-S.; Shiratsuchi, T.; Sugimoto, T.; Ryu, S.; Ku, J. H.; Watanabe, T.; Park, Y.; Aihara, Y.; Im, D.; Han, I. T. High-energy long-cycling all-solid-state lithium metal batteries enabled by silver−carbon composite anodes. *Nat. Energy* **2020**, *5*, 299−308.

(13) Wu, J.; Liu, S.; Han, F.; Yao, X.; Wang, C. Lithium/Sulfide All-Solid-State Batteries using Sulfide Electrolytes. *Adv. Mater.* **2021**, *33*, No. 2000751.

(14) Liu, G.; Weng, W.; Zhang, Z.; Wu, L.; Yang, J.; Yao, X. Densified Li_6PS_5Cl Nanorods with High Ionic Conductivity and Improved Critical Current Density for All-Solid-State Lithium Batteries. *Nano Lett.* **2020**, *20*, 6660−6665.

(15) Kim, M.; Pompizii, L.; Byun, J.; Coskun, A.; Choi, J. W. The challenge of corrosion in next-generation rechargeable metal batteries. *Chem* **2025**, *11*, No. 10266110.

(16) Oh, J.; Kim, J.; Bae, S.; Kim, H.; Lee, T.; Choi, S. H.; Park, G.; Ji, S.; Kim, K. J.; Choi, J. W. Comprehensive Analysis of Anode-Less Batteries with Lithiophilic Seeds in Liquid and Solid-State Electrolytes. *Adv. Energy Mater.* **2025**, *15*, No. e02711.

(17) Oh, J.; Lee, T.; Lee, N.; Sohn, Y.; Kim, J. Y.; Bae, K. Y.; Choi, S. H.; Choi, J. W. Kinetically Engineered Lithiophilic Dual-Metal Layers for Dendrite-Free, High-Energy Anode-Less All-Solid-State Batteries. *Battery Energy* **2025**, *4*, No. e70038.

(18) Wang, Y.; Raj, V.; Naik, K. G.; Vishnugopi, B. S.; Cho, J.; Nguyen, M.; Recker, E. A.; Su, Y.; Celio, H.; Dolocan, A.; Page, Z. A.; Watt, J.; Henkelman, G.; Tu, Q. H.; Mukherjee, P. P.; Mitlin, D. Control of Two Solid Electrolyte Interphases at the Negative Electrode of an Anode-Free All Solid-State Battery based on Argyrodite Electrolyte. *Adv. Mater.* **2025**, *37*, No. 2410948.

(19) Oh, J.; Choi, S. H.; Kim, H.; Kim, J. Y.; Lee, G.-J.; Bae, K. Y.; Lee, T.; Lee, N.; Sohn, Y.; Chung, W. J.; Choi, J. W. Lithio-amphiphilic nanobilayer for high energy density anode-less all-solid-state batteries operating under low stack pressure. *Energy Environ. Sci.* **2024**, *17*, 7932−7943.

(20) Lee, J. H.; Oh, S.-H.; Yim, H.; Lee, H.-J.; Kwon, E.; Yu, S.; Kim, J. S.; Song, J.; Koo, J.; Cho, J.; Kim, S. H.; Ryu, A.; Choi, S. H.; Kim, Y.; Im, G.; Choi, J.-W.; Yu, S.-H. Interfacial stabilization strategy via In-doped Ag metal coating enables a high cycle life of anode-free solid-state Li batteries. *Energy Storage Mater.* **2024**, *69*, No. 103398.

(21) Zhang, L.; Cui, R. H.; Jeong, H. S.; Shin, K. H.; Fu, H.; Lee, K. B.; Jo, S.; Hong, J.; Sohn, J. I. Thermodynamically-Favorable Tailored Au−F Interface for Uniform Lithium Deposition in Anode-Free Solid-State Batteries. *Adv. Energy Mater.* **2025**, *15*, No. e03394.

(22) Wang, Y.; Liu, Y.; Nguyen, M.; Cho, J.; Katyal, N.; Vishnugopi, B. S.; Hao, H.; Fang, Y.; Wu, N.; Liu, P.; Mukherjee, P. P.; Nanda, J.; Henkelman, G.; Watt, J.; Mitlin, D. Stable Anode-Free All-Solid-State Lithium Battery through Tuned Metal Wetting on the Copper Current Collector. *Adv. Mater.* **2023**, *35*, No. 2206762.

(23) Lee, J.; Choi, S. H.; Im, G.; Lee, K.-J.; Lee, T.; Oh, J.; Lee, N.; Kim, H.; Kim, Y.; Lee, S.; Choi, J. W. Room-Temperature Anode-Less All-Solid-State Batteries via the Conversion Reaction of Metal Fluorides. *Adv. Mater.* **2022**, *34*, No. 2203580.

(24) Sohn, Y.; Oh, J.; Lee, J.; Kim, H.; Hwang, I.; Noh, G.; Lee, T.; Kim, J. Y.; Bae, K. Y.; Lee, T.; Lee, N.; Chung, W. J.; Choi, J. W. Dual-Seed Strategy for High-Performance Anode-Less All-Solid-State Batteries. *Adv. Mater.* **2024**, *36*, No. 2407443.

(25) Jeon, S.-J.; Hwang, C.; Kim, H.-S.; Park, J.; Hwang, J.-Y.; Jung, Y.; Choi, R.; Song, M.-S.; Lee, Y. J.; Yu, J.-S.; Jung, Y.-C. Sonochemically Prepared Nanodot Magnesium Fluoride-Based Anodeless Carbon Substrate for Simultaneously Reinforcing Interphasial and Reaction Kinetics for Sulfide-Based All-Solid-State Batteries. *Adv. Energy Mater.* **2024**, *14*, No. 2402887.

(26) Jun, D.; Park, S. H.; Jung, J. E.; Lee, S. G.; Kim, K. S.; Kim, J. Y.; Bae, K. Y.; Son, S.; Lee, Y. J. Ultra-Stable Breathing Anode for Li-Free All-Solid-State Battery Based on Li Concentration Gradient in Magnesium Particles. *Adv. Funct. Mater.* **2024**, *34*, No. 2310259.

(27) Choi, S. H.; Baek, C. H.; Oh, J.; Lee, G.-J.; Kim, M.; Lee, H.; Yoo, D.-J.; Jung, Y. S.; Kim, K.; Yu, J.-S.; Cho, W.; Park, H.; Choi, J. W. Silver exsolution from Li-argyrodite electrolytes for initially anode-free all-solid-state batteries. *Nat. Commun.* **2025**, *16*, No. 5871.

(28) Chen, Y.; Wang, Z.; Li, X.; Yao, X.; Wang, C.; Li, Y.; Xue, W.; Yu, D.; Kim, S. Y.; Yang, F.; Kushima, A.; Zhang, G.; Huang, H.; Wu, N.; Mai, Y.-W.; Goodenough, J. B.; Li, J. Li metal deposition and stripping in a solid-state battery via Coble creep. *Nature* **2020**, *578*, 251−255.

(29) Liao, D. W.; Cho, T. H.; Sarna, S.; Jangid, M. K.; Kawakami, H.; Kotaka, T.; Aotani, K.; Dasgupta, N. P. Interfacial dynamics of carbon interlayers in anode-free solid-state batteries. *J. Mater. Chem. A* **2024**, *12*, 5990−6003.

(30) Suzuki, N.; Yashiro, N.; Fujiki, S.; Omoda, R.; Shiratsuchi, T.; Watanabe, T.; Aihara, Y. Highly Cyclable All-Solid-State Battery with Deposition-Type Lithium Metal Anode Based on Thin Carbon Black Layer. *Adv. Energy Sustainability Res.* **2021**, *2*, No. 2100066.

(31) Park, S. H.; Jun, D.; Jung, J. E.; Lee, S. G.; Lee, G. H.; Lee, Y. J. Clarification of Li deposition behavior on anodes with a porous interlayer in Li-free all-solid-state batteries. *J. Mater. Chem. A* **2022**, *10*, 21995−22006.

(32) Park, S. H.; Naik, K. G.; Vishnugopi, B. S.; Mukherjee, P. P.; Hatzell, K. B. Lithium Kinetics in Ag−C Porous Interlayer in Reservoir-Free Solid-State Batteries. *Adv. Energy Mater.* **2025**, *15*, No. 2405129.

(33) Xie, F.; Diallo, M. S.; Kim, H.; Tu, Q. H.; Ceder, G. The Microscopic Mechanism of Lithiation and Delithiation in the Ag/C Buffer Layer for Anode-Free Solid-State Batteries. *Adv. Energy Mater.* **2024**, *14*, No. 2302960.

(34) Jung, Y.-C.; Hwang, C.; Kwak, M.-J.; Jeon, S.-J.; Lee, Y. J.; Kwak, W.-J.; Kim, H.-S.; Kim, K.; Cho, W.; Yu, J.-S. On-site formation of silver decorated carbon as an anodeless electrode for high-energy density all-solid-state batteries. *J. Mater. Chem. A* **2023**, *11*, 25275−25282.

(35) Jun, D.; Jung, J. E.; Yim, H.; Kim, H.; Lee, S. G.; Kim, K. S.; Shim, S.; Kim, T. E.; Lee, Y. J. Solubility Does Not Matter: Engineered Anode Architectures Activates Cost-Effective Metals for Controlled Lithium Morphology in Li-Free all-Solid-State Batteries. *Adv. Energy Mater.* **2025**, *15*, No. e02956.

(36) Hong, S.-B.; Lee, Y.-J.; Kim, U.-H.; Bak, C.; Lee, Y. M.; Cho, W.; Hah, H. J.; Sun, Y.-K.; Kim, D.-W. All-Solid-State Lithium Batteries: Li^+−Conducting Ionomer Binder for Dry-Processed Composite Cathodes. *ACS Energy Lett.* **2022**, *7*, 1092−1100.

(37) Wang, Q.; Zhao, C.; Wang, S.; Wang, J.; Liu, M.; Ganapathy, S.; Bai, X.; Li, B.; Wagemaker, M. Clarifying the Relationship between the Lithium Deposition Coverage and Microstructure in Lithium Metal Batteries. *J. Am. Chem. Soc.* **2022**, *144*, 21961−21971.

(38) Chen, Y.; Li, M.; Liu, Y.; Jie, Y.; Li, W.; Huang, F.; Li, X.; He, Z.; Ren, X.; Chen, Y.; Meng, X.; Cheng, T.; Gu, M.; Jiao, S.; Cao, R. Origin of dendrite-free lithium deposition in concentrated electrolytes. *Nat. Commun.* **2023**, *14*, No. 2655.

(39) Jun, D.; Lee, J.-H.; Park, S. H.; Son, S.; Lee, J. H.; Lee, Y. J. Alloy Phase-Formation-Driven Lithium Deposition Pathways in Magnesium-Based Breathing Anodes for Long-Lasting Anode-Free All-Solid-State Batteries. *ACS Energy Lett.* **2026**, *11*, 2135−2142.

(40) Park, S. H.; Ayyaswamy, A.; Gjerde, J.; Andrews, W. B.; Vishnugopi, B. S.; Drakopoulos, M.; Vo, N. T.; Zhong, Z.; Thornton, K.; Mukherjee, P. P.; Hatzell, K. B. Filament-Induced Failure in Lithium-Reservoir-Free Solid-State Batteries. *ACS Energy Lett.* **2025**, *10*, 1174−1182.

(41) Kazyak, E.; Wang, M. J.; Lee, K.; Yadavalli, S.; Sanchez, A. J.; Thouless, M. D.; Sakamoto, J.; Dasgupta, N. P. Understanding the electro-chemo-mechanics of Li plating in anode-free solid-state batteries with *operando* 3D microscopy. *Matter* **2022**, *5*, 3912-3934.

https://doi.org/10.1021/acsenergylett.6c00964
ACS Energy Lett. 2026, 11, 5051−5060

(42) Hong, S.-B.; Lee, H.; Lee, Y.-J.; Kim, C.; Lee, Y. M.; Kim, U.-H.; Kim, D.-W. Unveiling Degradation Mechanisms of Sulfide-Based Composite Cathodes Supported by Digital-Twin Modeling: Dry Binder versus Wet Binder. *Energy Storage Mater.* **2026**, *86*, No. 104930.
(43) Hong, S.-B.; Jang, Y.-R.; Jung, Y.-C.; Cho, W.; Kim, D.-W. Sulfide-Based Flexible Solid Electrolyte Enhancing Cycling Performance of All-Solid-State Lithium Batteries. *ACS Appl. Energy Mater.* **2024**, *7*, 5193−5201.

https://doi.org/10.1021/acsenergylett.6c00964
ACS Energy Lett. 2026, 11, 5051−5060